Materials
Advances

Accepted Manuscript

This article can be cited before page numbers have been issued, to do this please use: R. K. Kushwaha, S. Jangid, P. Mishra, S. Sharma and R. P. Singh, *Mater. Adv.*, 2026, DOI: 10.1039/D5MA01057H.

ROYAL SOCIETY
OF CHEMISTRY

rsc.li/materials-advances

View Article Online
DOI: 10.1039/D5MA01057H

All data that support the findings of this study are available within the paper. Any data related to this paper may be requested from R.P.S. (rpsingh@iiserb.ac.in).

View Article Online
DOI: 10.1039/D5MA01057H

Journal Name

ARTICLE TYPE

Cite this: DOI: 00.0000/xxxxxxxxxx

Received Date
Accepted Date

DOI: 00.0000/xxxxxxxxxx

High Critical Temperature and Field Superconductivity in $Nb_{0.85}X_{0.15}$, (X = Ti, Zr, Hf) Alloys: Promising Candidates for Superconducting Devices

Roshan Kumar Kushwaha[a], Sonika Jangid[a], Priya Mishra[a], Suhani Sharma[a] and Ravi Prakash Singh*[a]

Niobium and its alloys with early transition metals have been extensively studied for their excellent superconducting properties. They have high transition temperatures, strong upper critical fields, and high critical current densities, making them ideal for superconducting applications such as SQUIDs, MRI, NMR, particle accelerators, and Qubits. Here we report a systematic investigation of as-cast Nb-rich alloys, $Nb_{0.85}X_{0.15}$ (X = Ti, Zr, Hf), using magnetization, electrical transport, and specific heat measurements. They exhibit strong type-II bulk superconductivity with moderate superconducting transition temperatures and upper critical fields. The estimated magnetic field-dependent critical current density lies in the range of 10^5–10^6 A/cm^2 across various temperatures, while the corresponding flux-pinning force density is on the order of GNm^{-3}, suggesting the potential of these materials for practical applications. Electronic-specific heat data reveal a strongly coupled, single, isotropic, nodeless superconducting gap. These Nb-rich alloys, characterized by robust superconducting properties, hold significant potential for applications in superconducting device technologies.

1 Introduction

Superconductivity is one of the most fascinating phenomena in condensed matter physics, offering both deep insights into quantum states of matter and broad technological potential. Among various superconducting materials, niobium (Nb)-based superconductors have emerged as highly sought-after materials in research due to their potential applications, characterized by high superconducting transition temperatures (T_c) and upper critical fields (H_{c2})[1–4]. Extensive studies have been conducted on Nb-based A-15[5–9] and Nb-T (T: early transition metals)[10] superconductors[11]. These materials show a wide array of physical properties, including large magnetoresistance[12], non-trivial band topology[13], and their ability to form wires[6,8] and superconducting joints[14,15]. Such characteristics make them promising candidates for advanced technologies[16–18]. In addition to industrial applications, Nb and Ta are widely recognized as suitable materials for superconducting radio frequency (SRF) cavities[19] and Josephson junctions[20,21], which facilitate the development of superconducting qubits[22,23]. Recent studies have shown that Ta-Zr[24] and Ta-Hf[25] alloys also exhibit promising superconducting properties. Owing to the high electropositivity of Hf and Zr, their alloys are considered strong candidates for meeting theoretical benchmarks aimed at enhancing qubit performance. Nb and Ta-based alloys, characterized by diverse crystal structures and physical properties, can provide a foundation for exploring similar compounds.

Among Nb-T alloys, Nb-Ti alloys[26–29] have achieved widespread commercial success in superconducting magnets and have also recently been studied under high pressure, setting new records for both T_c (= 19.1 K) and H_{c2} (= 19 T) among all alloys composed only of transition metals[30]. Additionally, Nb-Ti alloys with Nb content 50% or more are applicable in osseous implant devices, such as orthopedic and orthodontic implants[31]. Furthermore, Nb-Zr[32–37] and Nb-Hf[38–40] alloys are also decisive in the same context. Nb-Zr alloys also present significant advantages for SRF cavities, including higher transition temperature, which facilitates reduced energy dissipation and cryogenic costs. Their simplified phase diagrams enable easier processing and optimization, while a stable ZrO_2 native oxide enhances RF performance by minimizing quench-inducing defects[41]. In addition, the combination of high values T_c and H_{c2} with low surface resistance, the absence of nodes in the gap symmetry, metallic behavior, high thermodynamic critical field and superheating field, and material morphology[42] make these alloys excellent candidates for high-performance SRF cavities. However, most of the research on these Nb-based alloys has focused on the A15 phase; a detailed study of the cubic α-W structure, which is the same as pure niobium, is lacking. These alloys are expected to exhibit superior superconducting and physical properties, making them suitable for superconducting

---

[a] Department of Physics, Indian Institute of Science Education and Research Bhopal, Bhopal, 462066, India; Tel: XX XXXX XXXX; E-mail: rpsingh@iiserb.ac.in

View Article Online
DOI: 10.1039/D5MA01057H

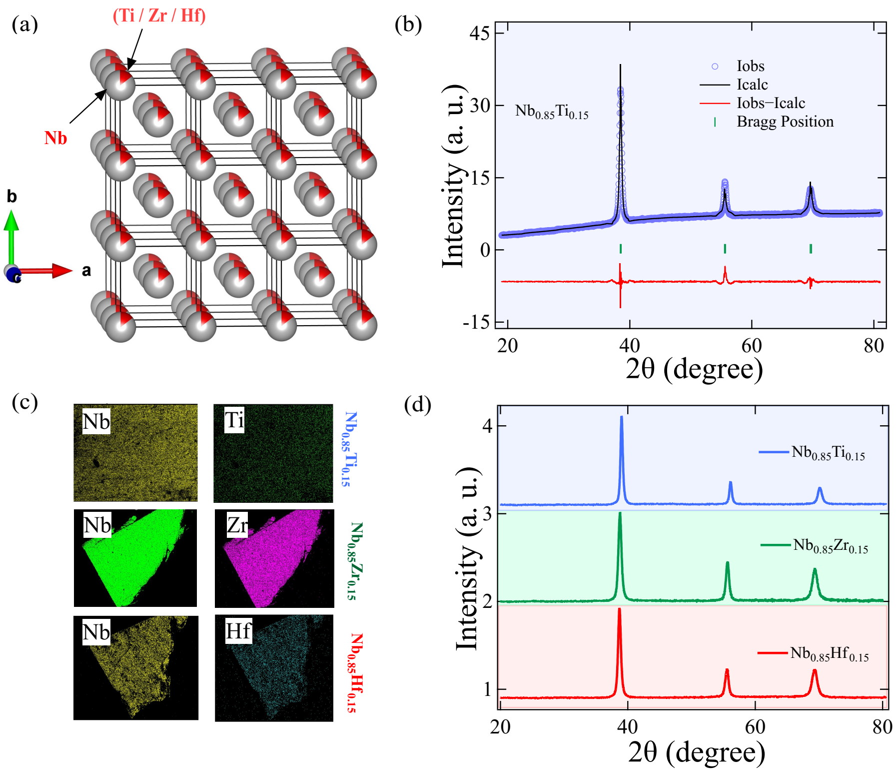

Fig. 1 (a) The bcc crystal structure of $Nb_{0.85}X_{0.15}$, (X = Ti, Zr, Hf) (b) Rietveld refinement of powder XRD pattern of Nb_6Ti alloy (c) Elemental mapping of $Nb_{0.85}X_{0.15}$ (X = Ti, Zr, Hf) alloys (d) Room temperature XRD patterns of $Nb_{0.85}X_{0.15}$, (X = Ti, Zr, Hf).

device applications. Therefore, a detailed study of niobium-rich alloys in α-W structure is crucial to identify promising candidates for practical applications.

In this paper, we have investigated the superconducting and normal-state properties of the Nb-rich family of alloys, $Nb_{0.85}X_{0.15}$ (nominal composition: Nb_6X, X = Ti, Zr, Hf). We substitute elements Ti (3d), Zr (4d), and Hf (5d) at the X site with a fixed Nb content. We perform a comparative analysis of superconducting and normal-state parameters derived from electrical resistivity, magnetization, and specific heat measurements, which remain relatively unexplored in the literature. Temperature-dependent magnetization loops yield critical current densities in the range of 10^5-10^6 A/cm^2, while the corresponding flux-pinning force density reaches several GNm^{-3}, underscoring their viability in technological applications. All alloys crystallized in the α-W bcc structure and show type-II strongly coupled superconductivity with the isotropic gap. The results obtained from this study on alloys, combined with a malleable morphology required for surface preparation, highlight their potential for further investigation in a thin film form for future applications in superconducting devices, such as single-photon detectors and superconducting qubits.

2 Materials and Methods

Polycrystalline samples of $Nb_{0.85}X_{0.15}$ (X = Ti, Zr, Hf) series were synthesized by arc melting in a pure argon atmosphere on a water-cooled copper hearth. The chamber was first evacuated to a base pressure and then backfilled to a partial pressure. This evacuation and backfilling cycle was performed three times to ensure a highly inert atmosphere. To ensure an oxygen-free environment, a Zr getter was used to absorb residual gaseous impurities. Stoichiometric amounts of the high-purity constituent elements (purity $\geq$ 99.9%) were melted together on a water-cooled copper hearth using a tungsten electrode. To achieve optimal homogeneity, the resulting ingot/button was flipped and remelted at least four to six times. The buttons were then cooled naturally on the copper hearth. The weight loss of the buttons after melting was observed to be negligible. The final samples used for various measurements were prepared by mechanically sectioning the arc-melted buttons using a low-speed diamond saw with a cutting fluid to prevent localized heating and structural damage, yielding pieces of the required dimensions. Phase purity and crystal structure were analyzed by room-temperature powder X-ray diffraction (XRD) using K_α (λ = 1.5406 Å) radiation using a PANalytical powder X-ray diffractometer. XRD refinement was performed using Fullprof Suite software[43]. Elemental composition and homogeneity were assessed by energy-dispersive X-ray analysis (EDXA) on a scanning electron microscope (SEM). Magnetization and AC susceptibility were measured using the Magnetic Property Measurement System (MPMS3). Full range magnetization loops at different temperatures were measured to calculate the critical current density on the rectangular slab of all alloys. Electrical resistivity was measured using the standard four-probe method in 1.9–300 K, while specific heat measurement was performed using the two-tau relaxation technique using the Physical Property Measurement System (PPMS).

View Article Online
DOI: 10.1039/D5MA01057H

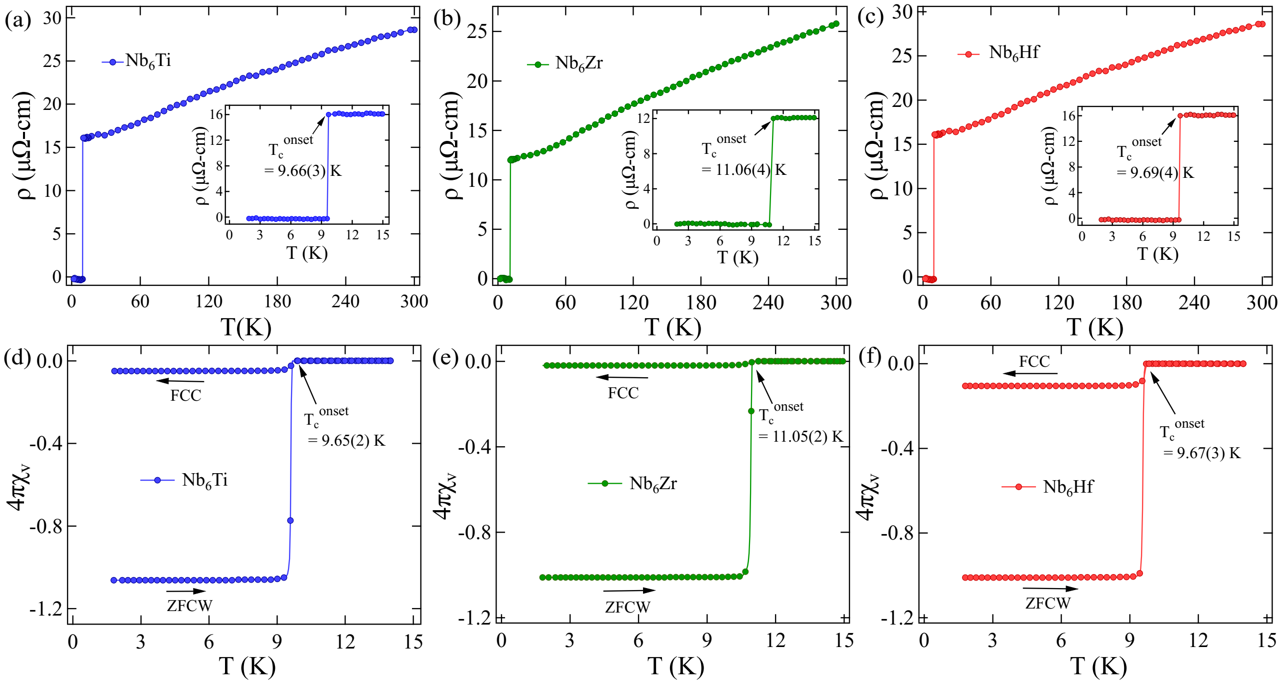

Fig. 2 Temperature-dependent electrical resistivity and the insets show zero drops in resistivity for (a) Nb_6Ti, (b) Nb_6Zr, (c) Nb_6Hf. Magnetization (corrected with demagnetization factor) in ZFCW and FCC mode at an applied field of 1 mT for (d) Nb_6Ti, (e) Nb_6Zr, and (f) Nb_6Hf, respectively.

3 Results and Discussion

3.1 Sample Characterization

All alloys are crystallized in the cubic structure α -W, and the crystal structure of $Nb_{0.85}X_{0.15}$ (X = Ti, Zr, Hf) is shown in Fig.1(a). The Rietveld refinement of the $Nb_{0.85}Ti_{0.15}$ alloy is shown in Fig.1(b). The elemental mapping of all alloys is shown in Fig.1(c). The XRD patterns of the polycrystalline samples of $Nb_{0.85}X_{0.15}$, (X = Ti, Zr, Hf) are shown in Fig.1 (d) and the lattice parameters determined from the refinement are summarized in Table1.

Table 1 Lattice parameters for $Nb_{0.85}X_{0.15}$, (X = Ti, Zr, Hf) obtained from XRD refinement.

Parameters	$Nb_{0.85}Ti_{0.15}$	$Nb_{0.85}Zr_{0.15}$	$Nb_{0.85}Hf_{0.15}$
a = b = c (Å)	3.306(8)	3.350(1)	3.349(5)
V_{cell} (Å^3)	36.16(6)	37.59(3)	37.56(4)

3.2 Electrical Resistivity

The temperature-dependent resistivity ($\rho(T)$) of Nb_6X (X = Ti, Zr, Hf) measured in the zero field confirms the transition temperatures T_c of 9.68(2), 11.06(4), 9.78(3) K, as shown in Fig.2(a), (b), and (c), and the insets show the corresponding zero drops in resistivity, respectively. The low residual resistivity ratio (RRR) is approximately 2, consistent with RRR for polycrystalline samples of some Heusler-type superconducting alloys[44].

3.3 Magnetization

The superconducting transition temperature of all alloys was confirmed through temperature-dependent magnetization measurements performed in zero field-cooled warming (ZFCW) and field-cooled cooling (FCC) modes under an applied magnetic field of 1 mT, where the quantity $4\pi\chi_v$ is corrected for the demagnetization factor. The results, presented in Fig.2(d), (e) and (f), indicate T_c values of 9.65 (2) K, 11.05 (2) K and 9.67 (3) K for Nb_6X (X = Ti, Zr, Hf), respectively. Temperature and field-dependent magnetization measurements were performed to determine the lower critical field ($H_{c1}(0)$) and the upper critical field ($H_{c2}(0)$). The H_{c1} values at each temperature were identified as the point where the magnetization curve deviates from the Meissner line (solid black line). The temperature dependence of H_{c1} was analyzed using the Ginzburg-Landau (GL) relation given

$$H_{c1}(T) = H_{c1}(0)\left[1-\left(\frac{T}{T_c}\right)^2\right] \tag{1}$$

which yields $H_{c1}(0)$ = 39.4 (2) mT, 107.4 (2) mT and 46.5 (3) mT for Nb_6X (X = Ti, Zr, Hf), respectively. The temperature dependence of H_{c1} is presented in Fig.3(a), (b), and (c), where the insets display magnetization magnetic field curves *vs.* at various temperatures for each sample. In addition, we estimate $H_{c2}(0)$ through magnetic field and temperature-dependent magnetization and resistivity measurements. The temperature dependence of H_{c2} was plotted and well fitted by the GL equation2, as shown in Fig.3(d), (e) and (f) for Nb_6X, (X = Ti, Zr, Hf), respectively.

$$H_{c2}(T) = H_{c2}(0)\left[\frac{1-(T/T_c)^2}{1+(T/T_c)^2}\right] \tag{2}$$

View Article Online
DOI: 10.1039/D5MA01057H

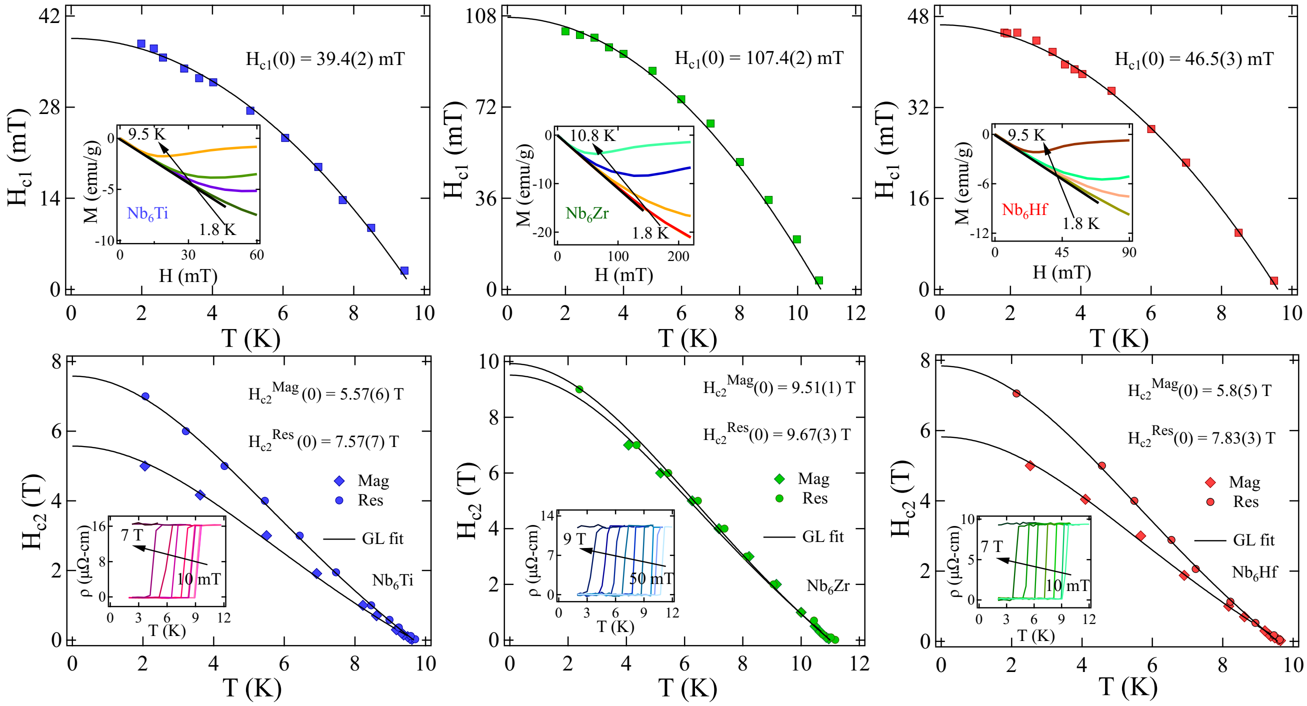

Fig. 3 Temperature-dependent lower critical field where the solid black curves represent G-L fit using Equation1 and the insets show the field-dependent magnetization curves for (a) Nb_6Ti, (b) Nb_6Zr, and (c) Nb_6Hf, respectively. Temperature-dependent profiles of the upper critical field, estimated from magnetization and resistivity, where the insets show magnetic field-dependent resistivity data for (d) Nb_6Ti, (e) Nb_6Zr, and (f) Nb_6Hf, respectively.

Equation2 yields estimated values of $H_{c2}(0)$ = 5.57(6), 9.51(1), and 5.81(5) T from magnetization and 7.57(7), 9.67(3) and 7.83(3) T from resistivity measurements for Nb_6X, (X = Ti, Zr, Hf), respectively, much higher than bulk Nb. The discrepancy between the values $H_{c2}(0)$ determined from the resistivity and magnetization measurements likely arises from the inherent limitations of the techniques, as well as their sensitivity to phenomena such as surface superconductivity and flux creep; however, for practical applications, the magnetization-derived value is more reliable, as it better reflects the bulk response of the sample.

The mechanisms behind Cooper pair-breaking when an external magnetic field is applied include the orbital pair-breaking effect and the Pauli limiting field effect. The orbital limiting field, $H_{c2}^{orb}(0)$, can be described by the Werthamer-Helfand-Hohenberg (WHH) model[45,46], which neglects the spin-orbit interaction and Pauli paramagnetism. According to the WHH model, $H_{c2}^{orb}(0)$ is expressed as

$$H_{c2}^{orb}(0) = -0.693\, T_c \left.\frac{dH_{c2}(T)}{dT}\right|_{T=T_c}. \tag{3}$$

By estimating the initial slopes of the H_{c2} vs T curves, $\frac{-dH_{c2}(T)}{dT}$ at $T = T_c$, we obtain the orbital limiting fields using Equation 3 as $H_{c2}^{orb}(0)$ = 4.13(6), 7.11(5), and 4.43(3) T for Nb_6X (X = Ti, Zr, Hf), respectively. For conventional superconductors, the Pauli limit field is given by the expression $H_{c2}^{P} = 1.86T_c$[47,48]. Using the T_c values obtained from magnetization measurements, we estimate the Pauli limiting fields H_{c2}^{P} as 17.94(3), 20.5(5), and 18.54(2) T for Nb_6X (X = Ti, Zr, Hf), respectively, which are significantly higher than the corresponding estimated values $H_{c2}(0)$. The coherence length $\xi_{GL}(0)$[49] can be estimated from $H_{c2}(0)$ using the relation $H_{c2}(0) = \frac{\Phi_0}{2\pi\xi_{GL}^2}$ where the magnetic flux quantum Φ_0 = 2.07 $\times 10^{-15}$ T m^2[49]. The penetration depth $\lambda_{GL}(0)$[50] is obtained from equation $H_{c1}(0) = \frac{\Phi_0}{4\pi\lambda_{GL}^2(0)}\left(ln\frac{\lambda_{GL}(0)}{\xi_{GL}(0)} + 0.12\right)$. The estimated values of $H_{c1}(0)$ and $H_{c2}(0)$ yield coherence lengths $\xi_{GL}(0)$ and penetration depths $\lambda_{GL}(0)$ as 76.9(1), 58.8(5) and 75.6(4) Å for $\xi_{GL}(0)$ and 1073(3), 615(2) and 975(4) Å for $\lambda_{GL}(0)$, for Nb_6X (X = Ti, Zr, Hf), respectively. The GL parameter defined as $k_{GL} = \frac{\lambda_{GL}(0)}{\xi_{GL}(0)}$, was found to be much higher than $\frac{1}{\sqrt{2}}$ for the three alloys, indicating strong type II superconductivity. In addition, the thermodynamic critical field ($H_c(0)$) is defined as $H_{c1}(0)\ H_{c2}(0) = H_c^2(0)\ ln(k_{GL})$. This yields the values of $H_c(0)$ = 288.6(2), 659.7(5), 325.6(8) mT for Nb_6X, (X = Ti, Zr, Hf), respectively. However, RF performance in SRF cavities using bulk Nb reaches the theoretical limit of $H_c(0) \sim 200\ mT$, our results indicate that the Nb_6X series has a higher thermodynamic critical field (> 200 mT), hence the higher superheating field ($H_{sh} \approx \frac{0.89}{\sqrt{k_{GL}}} H_c$)[51].

The Ginzburg-Levanyuk number (Gi) quantifies the strength of thermal fluctuations relative to vortex unpinning in type-II superconductors[52], which is described by the following expression

$$Gi = \frac{1}{2}\left(\frac{k_B \mu_0 \tau T_c}{4\pi\xi(0)^3 H_c^2(0)}\right)^2, \tag{4}$$

where τ is the anisotropy factor that is 1 for cubic Nb_6X, (X = Ti, Zr, Hf)). Using the estimated T_c, $\xi(0)$ and $H_c(0)$ of magne-

View Article Online
DOI: 10.1039/D5MA01057H

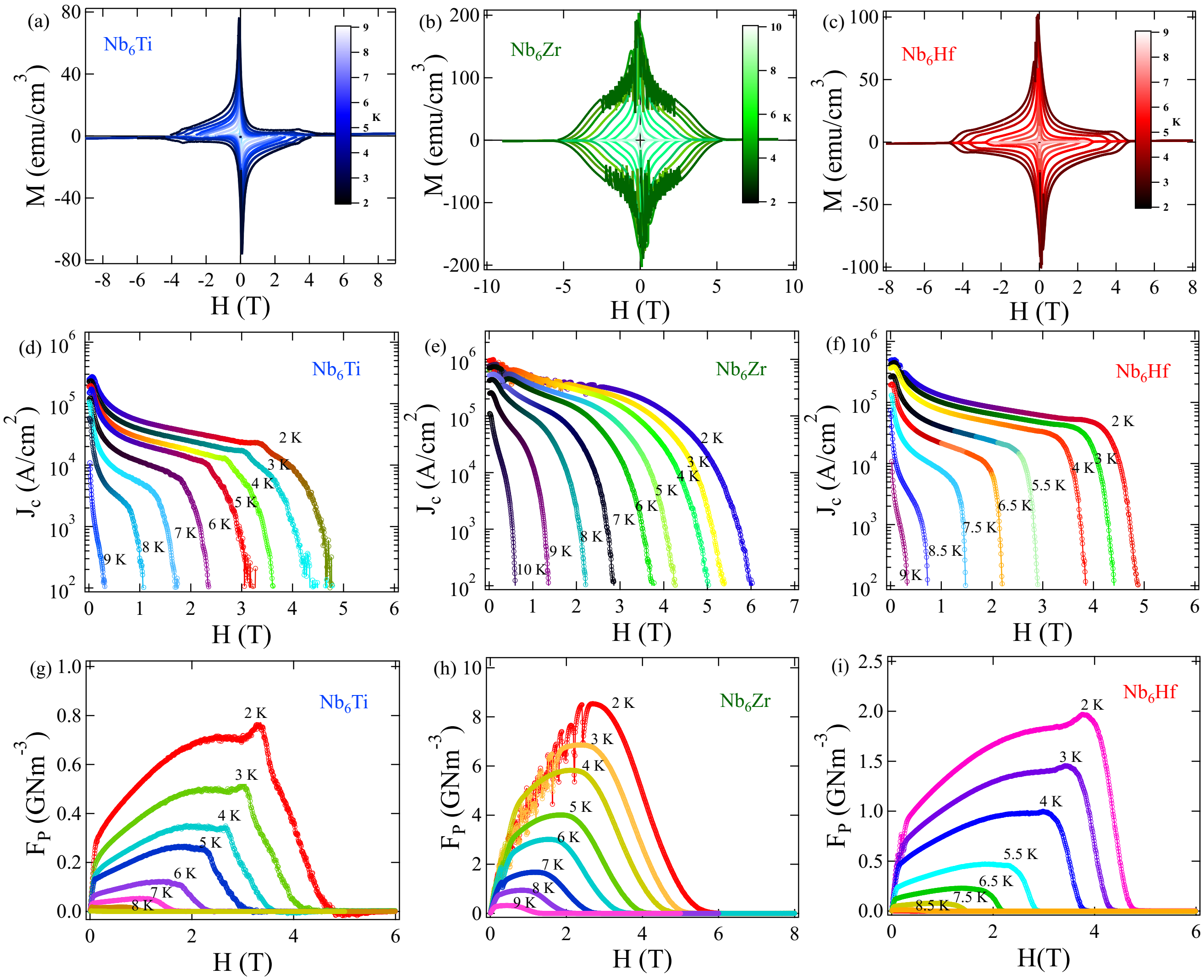

Fig. 4 (a), (b) and (c) M-H loops at different temperatures, whereas (d), (e) and (f) magnetic field dependent J$_c$ variation at different temperatures and (g), (h) and (i) Variation of flux pinning force with magnetic field for Nb$_6$X, (X = Ti, Zr, Hf), respectively.

tization measurement, we obtain Gi = 6.18(2) × 10^{-8}, 1.48(4) × 10^{-8}, 4.43(8) × 10^{-8} for Nb$_6$X, (X = Ti, Zr, Hf), respectively. These values are comparable to typical values Gi observed for low T_c superconductors (~10^{-8}). This suggests that thermal fluctuations do not contribute significantly to vortex unpinning in Nb$_6$X series[53].

3.4 Critical Current Density and Flux Pinning Force

Magnetic hysteresis loops (see Figs.5(a), (b), and (c)) of Nb$_6$X (X = Ti, Zr, Hf) series were measured at different temperatures to assess the critical current density (J_c) and its variation with magnetic field. Both Nb$_6$Zr and Nb$_6$Hf alloys show several low-field flux jumps in the M-H curves, as shown in Fig.5(b) and (c). These flux jumps weaken and disappear when the temperature rises above 4 K or the magnetic field exceeds 3 T. Usually, flux jump phenomena are common in these alloys because of the strong magnetic flux pinning, while Nb$_6$ Ti does not have a flux pinning force at all, suggesting a relatively weak flux pinning force. The magnetic flux pinning force inside the Nb$_6$Zr sample is strongest, reflecting the high-low field flux jumps. The irreversible field (H$_{irr}$) of all samples is evaluated from the corresponding M-H loops at different temperatures. H$_{irr}$ is the magnetic field above which vortice unpinning begins, and as the temperature increases, the irreversible fields of all samples decrease to various degrees. J_c is obtained by the Bean model[54] as described for J_c in the following equation:

$$J_c = \frac{20\,\Delta M}{w\left(1-\frac{w}{3l}\right)} \tag{5}$$

where, w and l are the width and length of the sample (l ≫ w) perpendicular to the direction of applied magnetic field, and ΔM is the width of the magnetization at the same magnetic field and Fig.5 (d), (e) and (f) show the magnetic field dependence of J_c for Nb$_6$X, (X = Ti, Zr, Hf), respectively. The $J_c(0)$ at T = 2 K is extracted as $J_c(0)$ = 2.48 × 10^5 A/cm^2, 1.02 × 10^6 A/cm^2 and 4.87 × 10^5 A/cm^2 for Nb$_6$ X (X = Ti, Zr, Hf), respectively. In addition, the pinning force density was calculated using the relation $F_p = \mu_0 H \times J_c$[55]. The variations of the flux pinning force

View Article Online
DOI: 10.1039/D5MA01057H

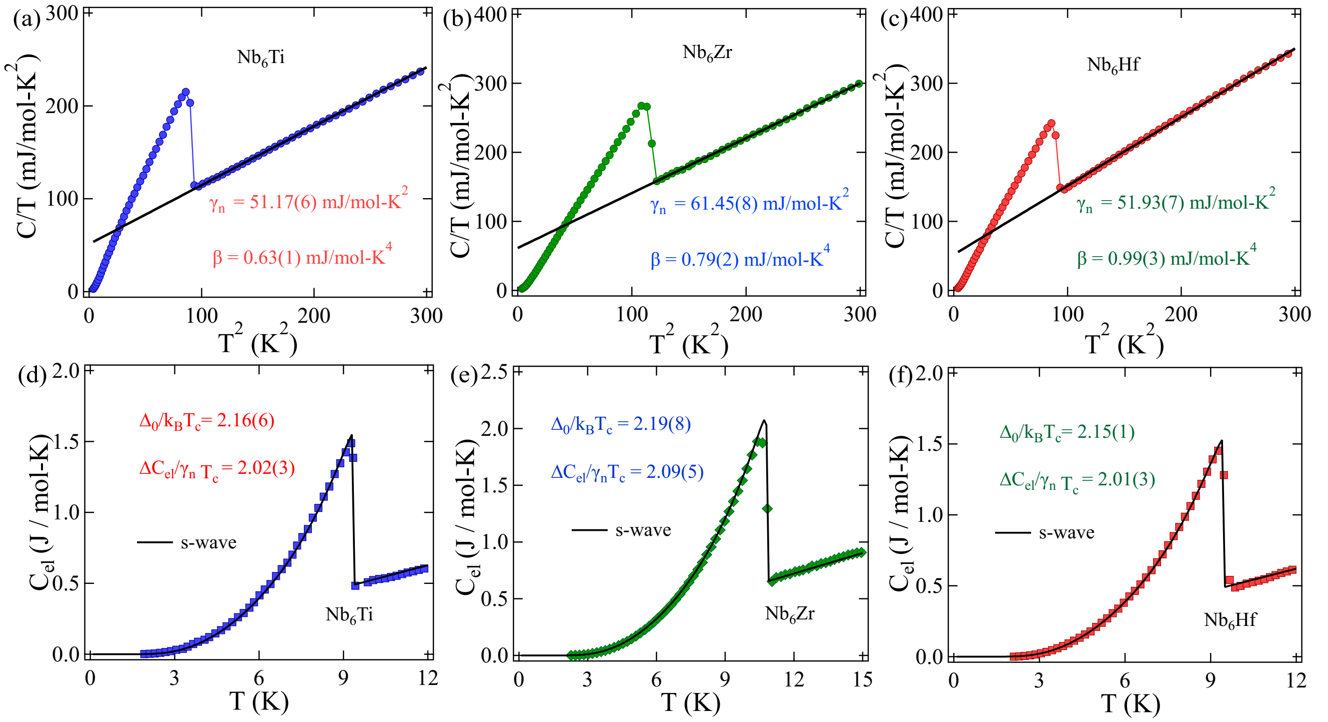

Fig. 5 (a), (b) and (c) C/T vs T^2 plot for Nb$_6$X, (X = Ti, Zr, Hf), respectively, where the solid black lines represent the Debye-Sommerfeld fitting represented by Equation6 (d), (e) and (f) C_{el} vs T plot for Nb$_6$X, (X = Ti, Zr, Hf), respectively, where solid black curves represent the s-wave model fit with BCS type single gap function.

density with magnetic field for Nb$_6$X, (X = Ti, Zr, Hf) are shown in Fig.5(g), (h) and (i), respectively. The density of the pinning force is obtained in the order of GNm^{-3} for this series, with the highest value obtained for Nb$_6$Zr due to the presence of low-field flux jumps, which is relatively low in Nb$_6$Hf and negligible in Nb$_6$Ti, suggesting the lowest value of the pinning force in Nb$_6$Ti. While flux jumps are commonly observed in Nb-based superconductors due to thermomagnetic instabilities, their absence in certain Nb alloys can be attributed to enhanced thermal conductivity and homogeneous flux pinning, which suppress abrupt vortex avalanches[56]. The critical current density and flux pinning force values for all alloys exceed the practical threshold value.

3.5 Specific Heat

Temperature-dependent specific heat measurements were performed for all samples without an external magnetic field to study the thermal properties of Nb$_6$X (X = Ti, Zr, Hf). Normal state C/T vs T^2 data were fitted using the Debye-Sommerfeld model represented by Equation6 and shown in Fig.5(a),(b) and (c) with solid black curves.

$$C/T = \gamma_n + \beta\ T^2 \tag{6}$$

where, γ_n is the Sommerfeld coefficient, β holds the phononic contributions to the specific heat. Fitting normal state specific heat data using Equation6 gives γ_n = 51.17(6), 61.45(8), 51.93(7) mJ mol^{-1}K^{-2} and β = 0.63(1), 0.79(2), 0.99(3) mJ mol^{-1}K^{-4} for Nb$_6$X (X = Ti, Zr, Hf), respectively. γ_n is related to the density of states on the Fermi surface $D_c(E_f)$ by the relation $\gamma_n = \left(\frac{\pi^2 k_B^2}{3}\right) D_c(E_f)$, where $k_B \approx 1.38 \times 10^{-23}$ J K^{-1}. $D_c(E_f)$ is estimated to be 21.7(1), 26.1(2), 22.1(1) states/eV f.u. for Nb$_6$X, (X = Ti, Zr, Hf), respectively. The debye temperature (θ_D) related to β as $\theta_D = \left(\frac{12\pi^4 RN}{5\beta_3}\right)^{1/3}$, where N is the number of atoms per formula unit and R is the molar gas constant (8.314 J mol^{-1} K^{-1}), which calculates θ_D = 277.8(9), 258.2(4), 239.5(3) K for Nb$_6$X, (X = Ti, Zr, Hf), respectively.

McMillan's model estimates the electron-phonon coupling strength from a dimensionless quantity λ_{e-ph}[57], which depends on the estimated values of θ_D and T_c as

$$\lambda_{e-ph} = \left[\frac{1.04 + \mu^* ln(\theta_D/1.45T_c)}{(1-0.62\mu^*)ln(\theta_D/1.45T_c) - 1.04}\right] \tag{7}$$

where μ^* is screened Coulomb repulsion, considering μ^* = 0.13 as described for transition metals[57], estimated λ_{e-ph} = 0.83(6), 0.92(4), 0.89(7) for Nb$_6$X, (X = Ti, Zr, Hf), respectively. It classifies them as strongly coupled superconductors. After subtracting the term $\beta\ T^3$ from total specific heat (C), the temperature-dependent electronic specific heat (C_{el}) was extracted for all samples and fitted with the isotropic single gap model, represented as solid black curves in Fig5(d), (e) and (f) and the quantity $\frac{\Delta C_{el}}{\gamma_n T_c}$ = 1.87(2), 1.79(5), 1.85(3) for Nb$_6$X, (X = Ti, Zr, Hf), respectively.

Further, C_{el} *vs.* T data can provide information about the symmetry of the superconducting gap around the Fermi surface, revealing the intricate pairing mechanism. Normalized entropy (S) in the superconducting region and C_{el} can be related as

$$\frac{C_{el}}{\gamma_n T_c} = t\ \frac{d\,(S/\gamma_n T_c)}{dt} \tag{8}$$

View Article Online
DOI: 10.1039/D5MA01057H

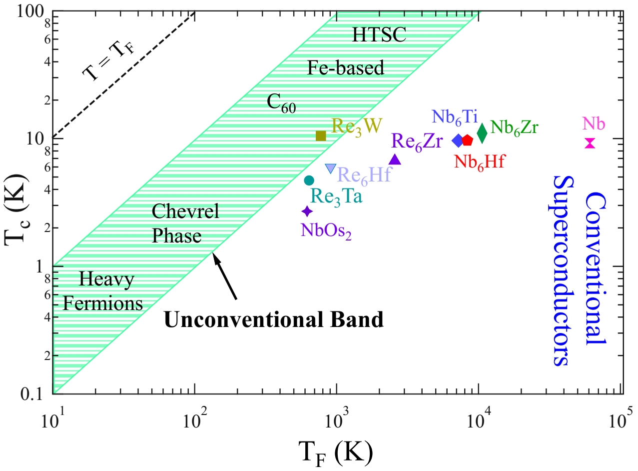

Fig. 6 Uemura plot defined by T_c and T_F for Nb_6X (X = Ti, Zr, Hf), where the green shaded region represents the unconventional band.

where $t = T/T_c$, the reduced temperature. Within the framework of the BCS approximation[58,59], the normalized entropy for a single BCS-like gap is defined by the following relation.

$$\frac{S}{\gamma_n T_c} = -\frac{6}{\pi^2}\Delta_T^s \int_0^\infty [f\ln(f) + (1-f)\ln(1-f)]dy \qquad (9)$$

where, $\Delta_T^s = \frac{\Delta(0)}{k_B T_c}$, $f(\xi) = [\exp(E(\xi)/k_B T)+1]^{-1}$ is the Fermi function, $E(\xi) = \sqrt{\xi^2 + \Delta^2(t)}$, where $E(\xi)$ is the energy of normal electrons measured relative to the Fermi energy, $y = \xi/\Delta(0)$, and $\Delta(t) = \tanh[1.82(1.018((1/t)-1))^{0.51}]$ represents the temperature-dependent superconducting energy gap. The solid black curves in Fig.5(d), (e), and (f) represent the fit to electronic specific heat data using a single isotropic nodeless gap model as described by Equation9, which provides the normalized superconducting gap values $\Delta(0)/k_B T_c$ = 2.16(1), 2.19(6), 2.15(3) for Nb_6X (X = Ti, Zr, Hf), respectively, which confirms the strong electron-phonon coupled superconductivity.

4 Normal State Properties and Uemura Classification

In this section, we have analytically solved a set of equations simultaneously to investigate electronic properties and discussed the Uemura classification of Nb_6X (X = Ti, Zr, Hf)[60]. The Sommerfeld coefficient (γ_n) is related to the quasiparticle number-density (n), defined as

$$\gamma_n = \left(\frac{\pi}{3}\right)^{2/3} \frac{k_B^2 m^* V_{f.u.} n^{1/3}}{\hbar^2 N_A} \qquad (10)$$

and Fermi velocity (v_F) is related to the electronic mean free path (l_e) and n by the expressions

$$l_e = \frac{3\pi^2\hbar^2}{e^2\rho_0 m*^2 v_F^2} \text{ and } n = \frac{1}{3\pi^2}\left(\frac{m^* v_F}{\hbar}\right)^3 \qquad (11)$$

respectively, where k_B is the Boltzmann constant, m^* is the effective mass of the quasiparticles, $V_{f.u.}$ is the volume of the formula unit, N_A is the Avogadro number and ρ_0 is the residual resistivity.

Within the dirty limit superconductivity, the BCS coherence length of a superconductor is much larger than the mean free path ($\frac{\xi_0}{l_e} \gg 1$), and the scattering of electrons with impurities and defects may affect the superconducting properties. The GL penetration depth (λ_{GL}) is related to the London penetration depth (λ_L) at absolute zero temperature followed by the expression

$$\lambda_{GL}(0) = \lambda_L\left(1 + \frac{\xi_0}{l_e}\right)^{1/2}, \text{where } \lambda_L = \left[\frac{m^*}{\mu_0 n e^2}\right]^{1/2} \qquad (12)$$

and BCS coherence length relates to GL coherence length and is expressed by

$$\frac{\xi_{GL}(0)}{\xi_0} = \frac{\pi}{2\sqrt{3}}(1 + \frac{\xi_0}{l_e})^{-1/2}. \qquad (13)$$

We have solved the above equations simultaneously and estimated the values of m^*, n, v_F, ξ_0, l_e, using the previously obtained values of γ_n, ρ_0, $\xi_{GL}(0)$ and $\lambda_{GL}(0)$. The Fermi temperature for an isotropic spherical Fermi surface is defined as

$$T_F = \frac{\hbar^2 k_F^{2/3}}{2\ m^* k_B} \quad , \qquad (14)$$

where $k_F = 3\pi^2 n$, the Fermi wave vector. The ratio T_c/T_F classifies superconductors into the conventional or unconventional category. According to Uemura et al.[60], the unconventional range $0.01 \leq \frac{T_c}{T_F} \leq 0.1$, shown by the green shaded band in Fig.6, whereas, T_c/T_F values for Nb_6X (X = Ti, Zr, Hf), lie outside this unconventional region. All superconducting and normal state parameters of Nb_6X (X = Ti, Zr, Hf), estimated from various techniques, are listed in Table 2. This comparison highlights that, despite variations in microstructure and alloying, Nb-based systems generally exhibit weak to moderate electronic correlations and conventional electron-phonon-mediated pairing. The similarity of T_c/T_F values across these families underscores that superconductivity in Nb_6X alloys is governed by the same fundamental mechanism, situating them firmly within the conventional regime while still offering competitive superconducting parameters for practical applications.

5 Discussion

Figure 7 presents a comparison of key superconducting parameters (T_c, H_{c2} and J_c) for Nb–T alloys α–W type (T = Ti, Zr, Hf) and other well-known compounds based on niobium. The data provide insight into the variation in superconducting behavior between different material classes. Niobium-based superconductors, especially binary alloys of Nb-T (where T = Ti, Zr, Hf) and Nb_3X compounds of type A15, represent two technologically significant families of low-temperature superconductors, each offering unique advantages tailored to specific operational demands. Nb-Ti alloys are widely used in commercial superconducting technologies due to their good thermal performance and suitability for wire manufacturing on a large scale[26,27,30,31]. Introducing alloying elements such as Ti or Zr into niobium enhances flux pinning capabilities while maintaining critical superconducting parameters, with transition temperatures ranging from 9 to 11 K and upper critical fields in the range of 6–14 T[68] at ambient pressure. Specifically, incorporating zirconium into niobium has been

View Article Online
DOI: 10.1039/D5MA01057H

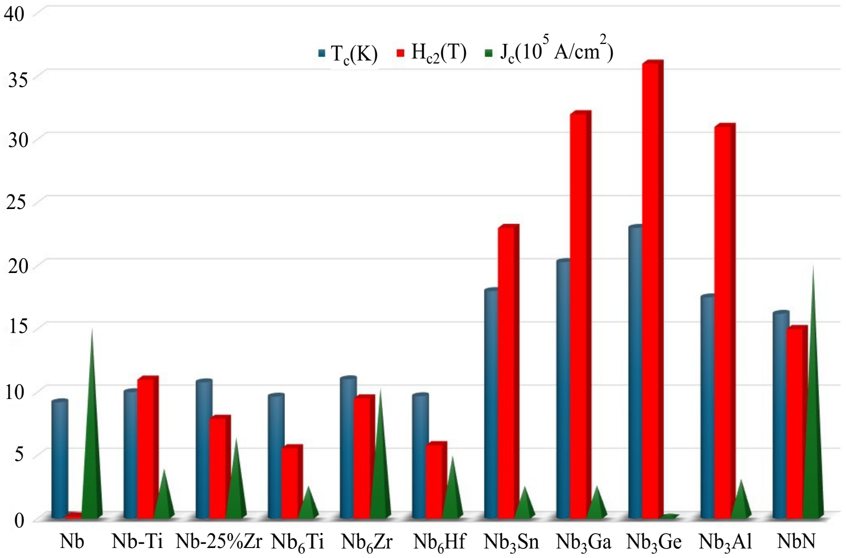

Fig. 7 Comparison of T_c, H_{c2}, J_c of Nb_6X, (X = Ti, Zr, Hf) with niobium[54] and its alloys[9,32–37,61–67].

Table 2 Superconducting and normal state parameters of Nb_6X, (X = Ti, Zr, Hf).

Parameters	unit	Nb_6Ti	Nb_6Zr	Nb_6Hf
T_c	K	9.65(2)	11.05(2)	9.67(3)
$H_{c1}(0)$	mT	39.4(2)	107.4(2)	46.5(3)
$H_{c2}(0)$	T	5.57(6)	9.51(1)	5.81(5)
$H_{c2}(0)^{Pauli}$	T	17.94(3)	20.5(5)	18.54(2)
$H_{c2}(0)^{orb}$	T	4.13(6)	7.11(5)	4.43(3)
$\xi_{GL}(0)$	Å	76.9(1)	58.8(5)	75.6(4)
$\lambda_{GL}(0)$	Å	1073(3)	615(2)	975(4)
$H_c(0)$	mT	288.6(2)	659.7(5)	325.6(8)
k_{GL}		13.9(5)	10.4(5)	12.9(4)
$\Delta C_{el}/\gamma_n T_c$		2.02(3)	2.09(5)	2.01(3)
$\Delta(0)/k_B T_c$		2.16(6)	2.19(8)	2.15(1)
θ_D	K	277.8(9)	258.2(4)	239.5(3)
λ_{e-ph}		0.83(6)	0.92(4)	0.89(7)
v_F	10^5 ms^{-1}	1.2(4)	1.4(6)	1.3(2)
n	10^{28} m^{-3}	13.4(2)	23.5(4)	15.6(3)
T_F	K	7234(4)	10595(25)	8346(8)
T_c/T_F		0.0013(3)	0.0010(3)	0.0011(5)
m^*/m_e		15.2(3)	15.1(2)	14.6(2)

shown to enhance surface superconductivity and radio-frequency characteristics, aided by the formation of a stable ZrO_2 surface layer and improved electron-phonon interactions[41]. In addition, alloys such as Nb-Zr and Nb—Hf exhibit strong resistance to radiation damage, making them particularly suitable for nuclear environments[69]. Recent computational studies suggest that irradiation promotes the formation of Nb-rich precipitates within Zr matrices, which adopt energetically favorable platelet morphologies. These structures contribute to enhanced microstructural integrity in nuclear fuel cladding materials under irradiation conditions[70–72].

In contrast, A15-type intermetallics such as Nb_3Sn, Nb_3Al, and Nb_3Ge demonstrate significantly enhanced superconducting characteristics, with critical temperatures (T_c) reaching up to 23 K and upper critical magnetic fields (H_{c2}) exceeding 30 T. These remarkable properties are mainly attributed to their distinctive crystal structure, characterized by quasi-one-dimensional chains of Nb atoms and a densely packed A_3B lattice[13]. This arrangement strengthens electron-phonon interactions near the Fermi level, thereby promoting superconductivity. However, these materials are inherently brittle and exhibit a high sensitivity to slight variations in composition, which presents challenges during processing. Beyond the superconducting parameters summarized in Fig7, prior studies have shown that microstructural refinement (e.g., grain size control in Nb_3Sn[61] and stacking fault regulation by nano-oxide particles in Nb_3Al[9]), defect density introduced by irradiation[73], and processing history such as hot rolling or equal channel angular pressing (ECAP) in NbTi[74] critically determine flux pinning and current-carrying capacity. These insights also contextualize the potential of Nb_6X alloys. The bulk properties observed here motivate future efforts in thin-film growth and characterization, where enhanced superconducting performance and device integration could be realized.

6 Conclusion

In summary, we have synthesized and characterized the Nb-rich series, $Nb_{0.85}X_{0.15}$ (nominal composition: Nb_6X, X = Ti, Zr, Hf), which crystallizes in a α-W bcc structure. We have thoroughly investigated their superconducting and normal state properties through XRD, electrical resistivity, magnetization, and specific heat measurements. All normal and superconducting state parameters follow nonmonotonic trends in Nb_6X series, since the X component is substituted by elements of Ti (3d), Zr (4d) and Hf (5d). The calculated critical current density from temperature-dependent magnetization loops has values in the range 10^5–10^6 A/cm^2 with a flux pinning force of the order of GNm^{-3}, which are good values for practical applications. All alloys have moderate transition temperatures and upper critical fields following isotropic nodeless superconducting gaps with strong electron-phonon coupling strength. The variation in spin-orbit coupling

View Article Online
DOI: 10.1039/D5MA01057H

strength from 3d to 5d elements, while maintaining a fixed Nb content, shows only a negligible influence on superconducting properties and gap symmetry, but it can provide further insight into the superconducting ground state and its relation to mechanical properties. Due to their morphological malleability and superior superconducting properties, this family of binary alloys holds significant promise, and dedicated thin-film studies will be essential to fully explore their technological potential in superconducting devices.

Conflicts of interest

There are no conflicts to declare.

Data availability

The data will be available on request.

Acknowledgement

R P S acknowledges the SERB Government of India for the Core Research Grant No. CRG/2023/000817. R K K acknowledges the UGC, Government of India, for providing a Senior Research Fellowship.

References

1 T. A. Coombs, Q. Wang, A. Shah, J. Hu, L. Hao, I. Patel, H. Wei, Y. Wu, T. Coombs and W. Wang, High-temperature superconductors and their large-scale applications, *Nat. Rev. Electr. Eng.*, 2024, 1–14.

2 R. Hampshire, The critical current-density of Nb-60 at% Ti and Nb-25 at% Zr superconductors in small magnetic fields, *J. Phys. D: Applied Physics*, 1974, **7**, 1847.

3 R. Scanlan, A. Malozemoff and D. Larbalestier, Superconducting materials for large scale applications, *Proceedings of the IEEE*, 2004, **92**, 1639–1654.

4 T. Priinits, A. Vargunin and A. Liivand, Peculiarities of niobium-based superconducting alloys in the light of crystal chemistry: A brief survey, *arXiv:2406.00817*, 2024.

5 G. Stewart, Superconductivity in the A15 structure, *Physica C*, 2015, **514**, 28–35.

6 N. Paudel, C. Tarantini, S. Balachandran, W. L. Starch, P. J. Lee and D. C. Larbalestier, Influence of Nb alloying on Nb recrystallization and the upper critical field of Nb_3Sn, *Phys. Rev. Mater.*, 2024, **8**, 084801.

7 K. Kinoshita, Crystal structures and properties of superconducting materials I, *Phase Transitions*, 1990, **23**, 73–250.

8 D. Rodrigues Jr and J. P. B. Machado, Development of $(Nb,Ta)_3Sn$ multifilamentary superconductor wire for high current applications, *Mat. Res.*, 2000, **3**, 99–103.

9 C. Yang, Z. Yu, W. Li, H. Zhang, J. Ren, W. Wang, Y. Zhang and Y. Zhao, New-route of flux pinning enhancement in Nb_3Al superconductor: density and orientation regulation of stacking faults by nano-oxide particles, *Supercond. Sci. Technol.*, 2025.

10 X. Xu, X. Peng, J. Rochester, M. Sumption, J. Lee, G. Calderon Ortiz and J. Hwang, The strong influence of Ti, Zr, Hf solutes and their oxidation on microstructure and performance of Nb3Sn superconductors, *J. Alloys Compounds*, 2021, **857**, 158270.

11 N. Paudel, C. Tarantini, S. Balachandran, W. L. Starch, P. J. Lee and D. C. Larbalestier, Influence of Nb alloying on Nb recrystallization and the upper critical field of Nb_3Sn, *Phys. Rev. Mater.*, 2024, **8**, 084801.

12 Q. Chen, Y. Zhou, B. Xu, Z. Lou, H. Chen, S. Chen, C. Wu, J. Du, H. Wang, J. Yang and M. Fang, Large Magnetoresistance and Nontrivial Berry Phase in Nb_3Sb Crystals with A15 Structure, *Chinese Physics Letters*, 2021, **38**, 087501.

13 M. Kim, C.-Z. Wang and K.-M. Ho, Topological states in A15 superconductors, *Phys. Rev. B*, 2019, **99**, 224506.

14 N. Banno, K. Kobayashi, A. Uchida and H. Kitaguchi, High-temperature-tolerable superconducting Nb-alloy and its application to Pb-and Cd-free superconducting joints between NbTi and Nb_3Sn wires, *Journal of Materials Science*, 2021, **56**, 20197–20207.

15 D. Patel, S.-H. Kim, W. Qiu, M. Maeda, A. Matsumoto, G. Nishijima, H. Kumakura, S. Choi and J. H. Kim, Niobium-titanium (Nb-Ti) superconducting joints for persistent-mode operation, *Sci. Rep.*, 2019, **9**, 14287.

16 B. Seeber, Commercially available superconducting wires, *Handbook of Applied Superconductivity*, 1998, 397–488.

17 B. Seeber, *Power Applications of Superconductivity: Handbook of Applied Superconductivity. Bristol, UK: Inst*, 1998.

18 S. S. Kalsi, Transmission and Distribution Conference and Exposition, 2003, pp. 1098–1101.

19 X. Fang, J.-S. Oh, M. Kramer, A. Romanenko, A. Grassellino, J. Zasadzinski and L. Zhou, Understanding mechanism of performance improvement in nitrogen-doped niobium superconducting radio frequency cavity, *Materials Research Letters*, 2023, **11**, 108–116.

20 D. Proch, P. Schmueser, W. Singer and L. Lilje, Niobium in superconducting RF cavities, *Niobium, Science and Technology*, 2001.

21 S. Casalbuoni, E. Knabbe, J. Kötzler, L. Lilje, L. Von Sawilski, P. Schmueser and B. Steffen, Surface superconductivity in niobium for superconducting RF cavities, *Nucl. Instrum. Methods Phys. Res. A*, 2005, **538**, 45–64.

22 N. P. de Leon, K. M. Itoh, D. Kim, K. K. Mehta, T. E. Northup, H. Paik, B. S. Palmer, N. Samarth, S. Sangtawesin and D. W. Steuerman, Materials challenges and opportunities for quantum computing hardware, *Science*, 2021, **372**, eabb2823.

23 A. P. Place, L. V. Rodgers, P. Mundada, B. M. Smitham, M. Fitzpatrick, Z. Leng, A. Premkumar, J. Bryon, A. Vrajitoarea, S. Sussman *et al.*, New material platform for superconducting transmon qubits with coherence times exceeding 0.3 milliseconds, *Nat. comm.*, 2021, **12**, 1779.

24 T. Klimczuk, S. Królak and R. J. Cava, Superconductivity of Ta-Hf and Ta-Zr alloys: Potential alloys for use in superconducting devices, *Phys. Rev. Mater.*, 2023, **7**, 064802.

25 P. K. Meena, S. Jangid, R. K. Kushwaha and R. P. Singh, Superconductivity with high upper critical field in Ta-Hf alloys, *Phys. Rev. Mater.*, 2023, **7**, 084801.

View Article Online
DOI: 10.1039/D5MA01057H

26 Y.-H. Hon, J.-Y. Wang and Y.-N. Pan, Composition/phase structure and properties of titanium-niobium alloys, *Materials transactions*, 2003, **44**, 2384–2390.

27 A. Cucciari, D. Naddeo, S. Di Cataldo and L. Boeri, NbTi: A nontrivial puzzle for the conventional theory of superconductivity, *Phys. Rev. B*, 2024, **110**, L140502.

28 C. Baker and J. Sutton, Correlation of superconducting and metallurgical properties of a Ti-20 at.% Nb alloy, *Philosophical Magazine*, 1969, **19**, 1223–1255.

29 P. D. Jablonski and D. C. Larbalestier, *Niobium-Titanium superconductors produced by powder metallurgy having artificial flux pinning centers*, 1993, US Patent 5,226,947.

30 J. Guo, G. Lin, S. Cai, C. Xi, C. Zhang, W. Sun, Q. Wang, K. Yang, A. Li, Q. Wu, Y. Zhang, T. Xiang, R. J. Cava and L. Sun, Record-High Superconductivity in Niobium-Titanium Alloy, *Adv. Mat.*, 2019, **31**, 1807240.

31 B. L. Pereira, C. M. Lepienski, V. Seba, G. Hobold, P. Soares, B. S. Chee, P. A. B. Kuroda, E. S. Szameitat, L. L. d. Santos, C. R. Grandini *et al.*, Titanium-niobium (Ti-xNb) alloys with high Nb amounts for applications in biomaterials, *Materials Research*, 2020, **23**, e20200405.

32 Z. Fan, E. Maras, M. Cottura, M.-C. Marinica and E. Clouet, Structure and coherency of bcc Nb precipitates in hcp Zr matrix from atomistic simulations, *Phys. Rev. Mater.*, 2024, **8**, 113601.

33 A. Junod, J. L. Jorda and J. Muller, Eliashberg analysis of the specific heat of $Nb_{0.75}Zr_{0.25}$, *Journal of low temperature physics*, 1986, **62**, 301–313.

34 W. Fietz, M. Beasley, J. Silcox and W. Webb, Magnetization of superconducting Nb-25% Zr wire, *Phys. Rev.*, 1964, **136**, A335.

35 T. G. Berlincourt, R. R. Hake and D. H. Leslie, Superconductivity at High Magnetic Fields and Current Densities in Some Nb-Zr Alloys, *Phys. Rev. Lett.*, 1961, **6**, 671–674.

36 A. Mirmefstein, A. Junod, E. Walker, B. Revaz, J. Genoud and G. Triscone, Mixed-State Specific Heat of the Type-II Superconductor $Nb_{0.77}Zr_{0.23}$ in Magnetic Fields up to B_{c2}, *Journal of superconductivity*, 1997, **10**, 527–535.

37 A. Junod, M. Roulin, B. Revaz, A. Erb and E. Walker, *The Gap Symmetry and Fluctuations in High-Tc Superconductors*, Springer, 2002, pp. 403–421.

38 C. Koch and R. Carpenter, Precipitates and fluxoid pinning in a superconducting Nb-Hf alloy, *Philosophical Magazine*, 1972, **25**, 303–320.

39 M. I. Bychkova, V. V. Baron and E. M. Savitskii, Physics and Metallurgy of Superconductors, 1970, pp. 74–79.

40 C. Koch, A. DasGupta, D. Kroeger and J. Scarbrough, The peak effect, summation problem, and magnetic history in a superconducting Nb-38 at.% |textHf alloy, *Philosophical Magazine B*, 1979, **40**, 361–387.

41 N. S. Sitaraman, Z. Sun, B. L. Francis, A. C. Hire, T. Oseroff, Z. Baraissov, T. A. Arias, R. G. Hennig, M. U. Liepe, D. A. Muller and M. K. Transtrum, Enhanced Surface Superconductivity of Niobium by Zirconium Doping, *Phys. Rev. Appl.*, 2023, **20**, 014064.

42 A.-M. Valente-Feliciano, Superconducting RF materials other than bulk niobium: a review, *Supercond. Sci. Technol.*, 2016, **29**, 113002.

43 J. Rodríguez-Carvajal, Recent advances in magnetic structure determination by neutron powder diffraction, *Physica B: Condensed Matter*, 1993, **192**, 55–69.

44 T. Klimczuk, C. H. Wang, K. Gofryk, F. Ronning, J. Winterlik, G. H. Fecher, J.-C. Griveau, E. Colineau, C. Felser, J. D. Thompson, D. J. Safarik and R. J. Cava, Superconductivity in the Heusler family of intermetallics, *Phys. Rev. B*, 2012, **85**, 174505.

45 E. Helfand and N. R. Werthamer, Temperature and Purity Dependence of the Superconducting Critical Field, H_{c2}. II, *Phys. Rev.*, 1966, **147**, 288–294.

46 N. R. Werthamer, E. Helfand and P. C. Hohenberg, Temperature and Purity Dependence of the Superconducting Critical Field, H_{c2}. III. Electron Spin and Spin-Orbit Effects, *Phys. Rev.*, 1966, **147**, 295–302.

47 A. B. Karki, Y. M. Xiong, I. Vekhter, D. Browne, P. W. Adams, D. P. Young, K. R. Thomas, J. Y. Chan, H. Kim and R. Prozorov, Structure and physical properties of the noncentrosymmetric superconductor Mo_3Al_2C, *Phys. Rev. B*, 2010, **82**, 064512.

48 J.-K. Bao, J.-Y. Liu, C.-W. Ma, Z.-H. Meng, Z.-T. Tang, Y.-L. Sun, H.-F. Zhai, H. Jiang, H. Bai, C.-M. Feng, Z.-A. Xu and G.-H. Cao, Superconductivity in Quasi-One-Dimensional $K_2Cr_3As_3$ with Significant Electron Correlations, *Phys. Rev. X*, 2015, **5**, 011013.

49 M. Tinkham, *Introduction to superconductivity*, Courier Corporation, 2004, vol. 1.

50 T. Klimczuk, F. Ronning, V. Sidorov, R. J. Cava and J. D. Thompson, Physical Properties of the Noncentrosymmetric Superconductor $Mg_{10}Ir_{19}B_{16}$, *Phys. Rev. Lett.*, 2007, **99**, 257004.

51 A. Gurevich, Enhancement of rf breakdown field of superconductors by multilayer coating, *Appl. Phys. Let.*, 2006, **88**, n/a.

52 O. Prakash, A. Thamizhavel and S. Ramakrishnan, Multiband superconductivity in $Lu_3Os_4Ge_{13}$, *Supercond. Sci. Technol.*, 2015, **28**, 115012.

53 A. E. Koshelev, K. Willa, R. Willa, M. P. Smylie, J.-K. Bao, D. Y. Chung, M. G. Kanatzidis, W.-K. Kwok and U. Welp, Melting of vortex lattice in the magnetic superconductor $RbEuFe_4As_4$, *Phys. Rev. B*, 2019, **100**, 094518.

54 C. P. Bean, Magnetization of high-field superconductors, *Reviews of modern physics*, 1964, **36**, 31.

55 E. Martínez, P. Mikheenko, M. Martínez-López, A. Millán, A. Bevan and J. S. Abell, Flux pinning force in bulk MgB_2 with variable grain size, *Phys. Rev. B*, 2007, **75**, 134515.

56 I. A. Golovchanskiy, A. V. Pan, T. H. Johansen, J. George, I. A. Rudnev, A. Rosenfeld and S. A. Fedoseev, Origin of magnetic flux-jumps in Nb films subject to mechanical vibrations and corresponding magnetic perturbations, *Phys. Rev. B*, 2018, **97**, 014524.

57 W. L. McMillan, Transition Temperature of Strong-Coupled

View Article Online
DOI: 10.1039/D5MA01057H

Superconductors, *Phys. Rev.*, 1968, **167**, 331–344.

58 J. Bardeen, L. N. Cooper and J. R. Schrieffer, Theory of Superconductivity, *Phys. Rev.*, 1957, **108**, 1175–1204.

59 H. Suhl and B. T. Matthias, Exchange Scattering in Superconductors, *Phys. Rev. Lett.*, 1959, **2**, 5–6.

60 Y. J. Uemura, V. J. Emery, A. R. Moodenbaugh, M. Suenaga, D. C. Johnston, A. J. Jacobson, J. T. Lewandowski, J. H. Brewer, R. F. Kiefl, S. R. Kreitzman, G. M. Luke, T. Riseman, C. E. Stronach, W. J. Kossler, J. R. Kempton, X. H. Yu, D. Opie and H. E. Schone, Systematic variation of magnetic-field penetration depth in high-T$_c$ superconductors studied by muon-spin relaxation, *Phys. Rev. B*, 1988, **38**, 909–912.

61 X. Xu, X. Peng, J. Rochester, M. Sumption, J. Lee, G. Calderon Ortiz and J. Hwang, The strong influence of Ti, Zr, Hf solutes and their oxidation on microstructure and performance of Nb3Sn superconductors, *Journal of Alloys and Compounds*, 2021, **857**, 158270.

62 J. D. Thompson, M. P. Maley, L. R. Newkirk and R. J. Bartlett, High-field properties and scaling in CVD-prepared Nb3Ge, *Journal of Applied Physics*, 1979, **50**, 977–982.

63 G. W. Webb, R. J. Tainsh and R. C. Dynes, Superconducting properties of sputtered Nb3Ge films, *Physical Review Letters*, 1973, **30**, 401–404.

64 R. Flükiger, H. Devantay and J. Müller, Superconducting properties of Nb3Ga prepared by different techniques, *IEEE Transactions on Magnetics*, 1981, **17**, 331–334.

65 L. M. Joshi, A. Verma, A. Gupta, P. K. Rout, S. Husale and R. C. Budhani, Superconducting properties of NbN film, bridge and meanders, *AIP Advances*, 2018, **8**, 055305.

66 T. Y. Jing, Z. Y. Han, Z. H. He, M. X. Shao, P. Li and Z. Q. Li, Quantum phase transition in NbN superconducting thin films, *Physical Review B*, 2023, **107**, 184515.

67 Anonymous, AIP Conference Proceedings, 2023, p. 030008.

68 Y. Shapira and L. J. Neuringer, Upper Critical Fields of Nb-Ti Alloys: Evidence for the Influence of Pauli Paramagnetism, *Phys. Rev.*, 1965, **140**, A1638–A1644.

69 G. He, *PhD thesis*, University of Oxford, 2020.

70 L. Goel, A. H. Mir, N. Naveen Kumar, P. V. Satyam, J. A. Hinks, S. E. Donelly and R. Tewari, Study on the dissolution of β-precipitates in the Zr–Nb alloy under the influence of Ne ion irradiation, *Microscopy*, 2021, **70**, 461–468.

71 L. Goel, Irradiation Induced Evolution of second phase precipitatesin Zr Nb based alloys.

72 C. d. F. Azevedo, Selection of fuel cladding material for nuclear fission reactors, *Engineering Failure Analysis*, 2011, **18**, 1943–1962.

73 M. Eisterer, *Neutron Irradiation: Introduced Defects in Various Superconductors*, IEEE CSC Presentation, 2018, Conference presentation.

74 I. Y. Moon, S.-J. Kim, H. W. Lee, J. Jung, Y.-S. Oh and S.-H. Kang, Investigation of the Correlation between Initial Microstructure and Critical Current Density of Nb-46.5 wt%Ti Superconducting Material, *Metals*, 2021, **11**, 777.